Atmospheric drying in Europe is human-induced and unprecedented in a 400-year context

Kerstin Treydte[a,b*], Laibao Liu[c+], Ryan S. Padrón[c,d+], Elisabet Martínez-Sancho[a,e], Flurin Babst[f], David C. Frank[g], Arthur Gessler[a,h], Ansgar Kahmen[i], Benjamin Poulter[j], Sonia I. Seneviratne[c], Annemiek Stegehuis[k], Robert Wilson[l,m], Laia Andreu-Hayles[m,n,o], Roderick Bale[p], Zdzislaw Bednarz[q], Tatjana Boettger[r], Frank Berninger[s], Ulf Büntgen[t,u,v], Valerie Daux[w], Isabel Dorado-Liñán[x], Jan Esper[y,u], Michael Friedrich[z], Mary Gagen[aa,bb], Michael Grabner[cc], Håkan Grudd[dd], Björn E. Gunnarsson[ee], Emilia Gutiérrez[e], Polona Hafner[ff], Marika Haupt[gg], Emmi Hilasvouri[hh], Ingo Heinrich[ii], Gerhard Helle[jj], Risto Jalkanen[kk], Högne Jungner[ll], Maarit Kalela-Brundin[mm], Andreas Kessler[a], Andreas Kirchhefer[nn], Stephan Klesse[a], Marek Krapiec[oo], Tom Levanič[ff,pp], Markus Leuenberger[qq], Hans W. Linderholm[rr], Danny McCarroll[aa], Valérie Masson-Delmotte[w], Slawomira Pawelczyk[ss], Anna Pazdur[ss], Octavi Planells[e], Rutile Pukiene[tt], Katja T. Rinne-Garmston[hh], Iain Robertson[aa], Antonio Saracino[uu], Matthias Saurer[a], Gerhard H. Schleser[vv], Kristina Seftigen[rr], Rolf T.W. Siegwolf[a], Eloni Sonninen[ll], Michel Stievenard[w], Elzbieta Szychowska-Krapiec[oo], Malgorzata Szymaszek[ww], Luigi Todaro[xx], John S. Waterhouse[yy], Martin Weigl-Kuska[zz], Rosmarie Weigt[aaa], Rupert Wimme[cc], Ewan J. Woodley[bbb], Adomas Vitas[ccc], Giles Young[hh], Neil J. Loader[aa]

*Kerstin Treydte
Swiss Federal Institute for Forest, Snow and Landscape Research WSL
Zürcherstrasse 111
CH-8903 Birmensdorf, Switzerland
Email: kerstin.treydte@wsl.ch

+ contributed equally as second authors

[a]Research Unit Forest Dynamics, Swiss Federal Research Institute for Forest, Snow and Landscape Research WSL, CH-8903 Birmensdorf, Switzerland;

[b]Oeschger Centre for Climate Change Research, University of Bern, CH-3012 Bern, Switzerland;

[c]Institute for Atmospheric and Climate Science, ETH Zurich, 8092 Zurich, Switzerland;

[d]Research Unit Mountain Hydrology and Mass Movements, Swiss Federal Research Institute for Forest, Snow and Landscape Research WSL, CH-8903 Birmensdorf, Switzerland;

[e]Department of Biological Evolution, Ecology and Environmental Sciences, University of Barcelona, 08028 Barcelona, Spain

[f]School of Natural Resources and the Environment, University of Arizona, Tucson AZ 85719, USA;

[g]Laboratory of Tree Ring Research, University of Arizona, Tucson AZ 85719, USA;

[h]Department of Environmental Systems Sciences, ETH Zurich, 8092 Zurich, Switzerland;

[i]Department of Environmental Sciences – Botany, University of Basel, 4056 Basel, Switzerland;

[j]Earth Sciences Division, Biospheric Sciences Laboratory, NASA Goddard Space Flight Center, Greenbelt MD 20771, USA;

[k]Laboratoire de Géologie, IPSL, CNRS UMR 8538, École Normale Supérieure, PSL University, Paris, France.

[l]School of Earth & Environmental Sciences, University of St. Andrews, KY16 9TS St. Andrews, United Kingdom;

[m]Tree Ring Laboratory, Lamont-Doherty Earth Observatory, Columbia University, New York, NY 10964, USA;

[n]Centre for Research on Ecology and Forestry Applications CREAF, 08193 Barcelona, Spain;

[o]ICREA, 08010 Barcelona, Spain;

[p]University of Wales Trinity Saint David Swansea SA1 8PH, United Kingdom;

[q]Department of Forest Biodiversity, Agricultural University, 31-425 Krakow, Poland;

[r]Department of Catchment Hydrology, Helmholtz Centre for Environmental Research UFZ, 06120 Halle, Germany;

[s]Department of Forest Sciences, University of Helsinki, 00014 Helsinki, Finland;

[t]Department of Geography, University of Cambridge, Cambridge CB2 3EN, United Kingdom;

[u]Global Change Research Institute (CzechGlobe), Czech Academy of Sciences, 60 300 Brno, Czech Republic;

[v]Department of Geography, Faculty of Science, Masaryk University, 611 37 Brno, Czech Republic;

[w]Laboratoire des Sciences du Climat et de l'Environnement, CEA-CNRS-Université de Versailles Saint-Quentin, 91191 Gif-sur-Yvette, France;

[x]Systems and Natural Resources Department, Universidad Politécnica de Madrid, 20840 Madrid, Spain;

[y]Department of Geography, Johannes-Gutenberg University, 55128 Mainz, Germany;

[z]University of Hohenheim, Hohenheim Gardens (772), 70599 Stuttgart, Germany;

[aa]Department of Geography, Swansea University, Swansea SA2 8PP, United Kingdom;

[bb]WWF-UK, United Kingdom;

[cc]Institute of Wood Technology and Renewable Resources, University of Natural Resources and Life Sciences BOKU Vienna, 3430 Tulln, Austria;

[dd]Swedish Polar Research Secretariat, Abisko Scientific Research Station, 98107 Abisko, Sweden;

[ee]Stockholm Tree Ring Laboratory, Department of Physical Geography, Stockholm University, 10691 Stockholm, Sweden;

[ff]Department of Yield and Silviculture, Slovenian Forestry Institute, 1000 Ljubljana, Slovenia;

[gg]Department of Isotope Hydrology, Helmholtz Centre for Environmental Research UFZ, 06120 Halle, Germany;

[hh]Natural Resources Institute Finland (Luke), 00790 Helsinki, Finland;

[ii]Deutsches Archäologisches Institut Berlin;

[jj]Section 4.3 Climate Dynamics and Landscape Evolution, German Research Centre for Geosciences GFZ, 14473 Potsdam, Germany;

[kk]Silva Lapponica, 96460 Rovaniemi, Finland;

[ll]Laboratory of Chronology, University of Helsinki, 00014 Helsinki, Finland;

[mm]Forestry Museum, 92132 Lycksele, Sweden;

[nn]Dendroøkologen, Skogåsvegen 6, 9011 Tromsö, Norway;

[oo]Faculty of Geology, Geophysics and Environmental Protection, AGH University of Science and Technology, 30-059 Krakow, Poland;

[pp]Faculty of Mathematics, Natural Sciences and Information Technologies, University of Primorska, SI-6000 Koper, Slovenia;

[qq]Climate and Environmental Physics Division and Oeschger Centre for Climate Change Research, University of Bern, 3012 Bern, Switzerland;

[rr]Department of Earth Sciences, University of Gothenburg, 40530 Gothenburg, Sweden;

[ss]Division of Geochronology and Environmental isotopes, Institute of Physics – CSE, Silesian University of Technology, 44-100 Gliwice, Poland;

[tt]The State Scientific Research Institute Nature Research Centre, 08412 Vilnius, Lithuania;

[uu]Department of Agricultural Sciences, University of Naples Federico II, I-80055 Portici-Napoli, Italy;

[vv]Institute of Bio- and Geosciences Agrosphere (IBG-3), Research Centre Julich GmbH, 52425 Julich, Germany;

[ww]Academic Secondary School, SUT 44-100 Gliwice, Poland;

[xx]School of Agriculture, Forest, Food and Environmental Sciences (SAFE), University of Basilicata I-85100 Potenza, Italy;

[yy]School of Life Sciences, Anglia Ruskin University, Cambridge CB1 1PT, United Kingdom;

[zz]Austrian Forest Products Research Society, 1030 Vienna, Austria;

[aaa]Laboratory of Atmospheric Chemistry, Paul Scherrer Institute, CH-5232 Villigen, Switzerland;

[bbb]Geography, College of Life and Environmental Sciences, University of Exeter, Exeter EX4 4RJ, United Kingdom;

[ccc]Centre of Environmental Research, Vytautas Magnus University, 44248 Kaunas, Lithuania;

Abstract

Vapor pressure deficit (VPD) represents the desiccation strength of the atmosphere that fundamentally affects evapotranspiration, ecosystem functioning and vegetation carbon uptake. Its spatial variability and long-term trends under natural *versus* human-influenced climate are poorly known but are essential for predicting future effects on natural ecosystems and human societies such as crop yield, wildfires, and health. We combine regionally distinct reconstructions of pre-industrial summer VPD variability from Europe's largest tree-ring oxygen-isotope network with observational records and Earth System Model simulations with and without human forcing included. We demonstrate that an intensification of atmospheric drying during the recent decades across different European target regions is unprecedented in a pre-industrial context and that it is attributed to human influence with more than 98% probability. The magnitude of this trend is largest in Western and Central Europe and the Alps & Pyrenees, and smallest in southern Fennoscandia. In view of the extreme drought and compound events of the recent years, further atmospheric drying poses an enhanced risk on vegetation, specifically in the densely populated areas of the European temperate lowlands including tree survival, forest resilience in natural and urban ecosystems, and food production.

Vapor pressure deficit, VPD, represents the difference between the amount of moisture that the air can hold at saturation (saturation vapor pressure, e_S) and its actual moisture content (actual vapor pressure, e_a) at any given time[1]. In a warming atmosphere e_s

increases, whereas changes in e_a are less uniform. The latter is because the vapor content of the atmosphere is driven by complex ocean-land–atmosphere water exchange mechanisms and recycling processes, i.e., the rate at which vapor is supplied to the atmosphere via both ocean evaporation and land surface evapotranspiration, and the strength of this ocean-land-atmosphere coupling[2]. High VPD can cause increased rates of water loss from soils and subsequent heating of the terrestrial surfaces via soil moisture-temperature feedback mechanisms[3,4]. VPD as a climate variable is therefore of fundamental ecological and socio-economic importance due to its effects on evapotranspiration and surface heat fluxes and, coupled with heatwaves, amplification of drought events with severe consequences on e.g., vegetation functioning[5], crop yield[6] and subsequently human health[7].

A general increase in VPD over the past decades has already been reported at a global scale[8], accelerating soil drought[9,10], plant water stress[11], vegetation mortality[12,13] and forest fires[14]. Its spatial evolution, long-term natural background variability and potential attribution to human influence are, however, still unclear. In consequence uncertainties in predictions of future VPD variability and its effects on the coupled carbon-water cycle and surface climate feedbacks by Earth System Models (ESMs) are also high.

We combine for the first-time empirical proxy data covering 400 years of pre-industrial and recent summer VPD variability with meteorological observations and ESM simulations to investigate spatio-temporal VPD patterns across Europe and understand their natural *versus* human-induced variability. This knowledge will contribute to reducing uncertainties in simulating future climate scenarios and help estimating the potential threat of high VPD levels to ecosystems, economies, and societies.

Empirical proxy data are represented by a European network of oxygen isotope ratios ($\delta^{18}O$) in tree rings from 45 sites that span a latitudinal gradient from northern Fennoscandia to the Mediterranean (Fig. 1). This network is unprecedented in terms of spatial coverage, number of sites, and composition of annually resolved multi-century long $\delta^{18}O$ chronologies. Sites range from temperate lowland over boreal and alpine to Mediterranean climates and contain seven tree genera, with oaks and pines being most represented (Fig. 1, Table S1). While coniferous sites are distributed across the whole network, broadleaf sites concentrate in the mid latitudes of western and eastern central Europe.

We explicitly utilize pure tree-ring $\delta^{18}O$ records instead of combining them with $\delta^{13}C$ records which was previously done for hydroclimatic reconstruction[15]. While combining both may be appealing due to their potentially strong inter-correlation in the high-frequency domain[16], long-term trends in $\delta^{13}C$ records can be biased by non-climatic effects in the industrial period (20th/21st century) due to a response of stomatal conductance to the increase in atmospheric CO_2 concentration[17,18]. Further, $\delta^{13}C$ records are sensitive to tree size and stand dynamics, while tree-ring $\delta^{18}O$ records are less sensitive to these factors[19]. Therefore, non-climatic trends are minimal to absent in pure tree-ring $\delta^{18}O$ records[20,21,22], and long-term climatic variation is preserved with much higher certainty.

Tree-ring $\delta^{18}O$ records have proven to be a particular robust climate proxy in temperate environments where traditional tree-ring parameters such as tree-ring width or maximum latewood density often underperform in recording hydroclimatic information[22]. They reflect the $\delta^{18}O$ variations of precipitation and soil water taken up by the roots, modified by a combination of climatic and physiological processes[23,24,25].Along these processes, evaporative enrichment of the heavy ^{18}O isotope along the atmosphere-soil-tree continuum is a key effect in generating a VPD-sensitive tree-ring $\delta^{18}O$ signature[26]. While the potential of tree-ring $\delta^{18}O$ to record VPD signals has been demonstrated[27,28,29,30,31], no robust reconstruction attempt has been made with the aim of placing recent VPD variability in a pre-industrial context.

Our spatially and temporally robust reconstructions of summer VPD variability for different independent European target regions combined with meteorological records and ESM simulations allow us to explore the following questions: 1) Is the increase in VPD observed across large parts of Europe in recent decades unprecedented in the pre-industrial context, and if so, 2) is it likely attributable to human-induced climate change? This is done by comparing the range and variability of i) reconstructed VPD values for the preindustrial period and ESM simulations without human induced forcing with ii) recent observations of VPD and ESM results including human forcing and implementing systematic attribution assessment[32].

Results

Network response to climate

The distribution of mean $\delta^{18}O$ values across the network represents the geographic location of the sites along latitudinal, longitudinal, and altitudinal gradients, with the effect of geographical location exceeding any effect of species (Supplementary text, Table S1 and Fig. S1). Climate signals recorded in the individual site chronologies are consistent across the geographical range of the network, with highest correlations observed with VPD (Fig. S2). Summer climate conditions (June to August, JJA) during the year of ring formation are the key driver of tree-ring $\delta^{18}O$ variability for both deciduous species and conifers, with climatic conditions in the year before ring formation being of minor relevance (Fig. S2). The strength of the relationship is not affected by the geographic location (Fig. S3) nor the general climatic conditions represented by the long-term means of various climate variables (Fig. S4), except at the southern (Mediterranean) and north-western edge of the network. Summer VPD was selected as the target variable for climate reconstruction due to its i) strongest spatial and temporal robustness across the network (Fig. 2a, Table S2, Fig. S2), and ii) relevance as a climatic and eco-physiological variable.

Spatio-temporal robustness of the summer VPD signal at the European scale

Fuzzy cluster analysis revealed grouping of the site $\delta^{18}O$ chronologies in five distinctly different geographic regions (Fig. 1, Fig. S5): northern Fennoscandia (NF), southern

Fennoscandia (SF), western Europe (WE), eastern central Europe (ECE), and the Alps & Pyrenees (AP). For subsequent nested principal component (PC) analysis, only chronologies that contributed >75% to the corresponding cluster were retained to ensure an independence between the regional reconstructions. The common variance explained by PC1 (common period of overlap 1920-1994) varied between 61% for WE, 64% for ECE, 61% for AP, 62% for SF, and 45% for NF.

Spatial correlation fields calculated between nested PC1 of each regional cluster and gridded summer VPD data confirmed the spatial coherence of the VPD signal recorded in tree-ring $\delta^{18}O$ on a continental scale (Fig. 2). All five geographic regions corresponded spatially to the areas with the highest correlations (Fig. 2b-f). For NF, however, the strength and spatial extent of the correlation with summer VPD was less pronounced compared to the other regions. Dipole-like correlation patterns emerged between eastern central Europe and Fennoscandia (Fig. 2d, e) and between southwestern and eastern Europe (Fig. 2c).

The strength and temporal robustness of the summer VPD signal in our tree-ring $\delta^{18}O$ proxies further increased when calculated for the regional PC1 records (Fig. S6). Particularly the WE record displayed exceptionally high correlations ($p<0.01$) for the full calibration period 1920-2000 ($r_{full}=0.79$), as well as for the early (1920-1960) and late (1961-2000) periods separately ($r_{early}=0.78$ and $r_{late}=0.82$). The ECE records also showed highly significant ($p<0.01$) and temporally stable correlations ($r_{full}=0.65$; $r_{early}=0.67$, $r_{late}=0.63$), followed by the SF record ($r_{full}=0.64$), with an increase of the correlations from the early to the late period (r_{early}=0.52, r_{late}=0.72) ($p<0.01$). Also, for the AP record, correlations were highly significant ($p<0.01$) (r_{full}=0.61) and robust over time (r_{early}=0.65, r_{late}=0.60). The NF record showed lowest, though still highly significant correlations, but with differences between the full *versus* split period values (r_{full}=0.42; $p<0.05$; r_{early}: 0.59, r_{late}: 0.52; $p<0.01$).

The robustness of the summer VPD signal through time as evaluated by calibration-verification statistics (Table S3, Fig. S6) allowed the development of regional reconstructions (Fig. 3). This was done by scaling the spliced regional PC1 nests to their VPD target over the full 1920-2000 calibration period (see Methods). Particularly the WE record yielded excellent reconstruction skills (Table S3, Fig. S6) and the signal was also robust in ECE, SF and AP. While for NF R^2-values were also still significant, other calibration-verification statistics failed (Table S3), indicating inconsistencies specifically in the long-term trends (Fig. S6). This prevented the creation of a robust reconstruction for NF. While our reconstructions end in the 2000s, the strong calibration-verifications statistics and scaling of the proxy to the variance and mean of the observations justified a direct combination with observational VPD in the period 1991-2020.

Unprecedented VPD increase in the pre-industrial context and its attribution to human influence

Historical periods of reconstructed dry and moist atmospheric summer conditions expectedly varied between the four regions and only few common patterns appeared

(Fig. 3): A transition from dry to moist conditions in the early 1600s until the 1640s appeared in all target regions; relatively moist conditions occurred during the 1670s to 1720s in all regions except SF, and from the 1730s to 1750 in WE and ECE, with comparably dry conditions in SF and AP. Another short dry period occurred at the end of the 19th century in all regions though less distinct in AP. In the early 20th century, a period with relatively high VPD levels appeared in all four regions in the late 1940s/early 1950s, albeit less distinct in SF, followed by moist conditions in the 1970s/early 1980s except SF. The most outstanding single extreme in the 400-year context was 1709 (Fig. 3). This was the year with the lowest atmospheric moisture demand in SF and WE. It is also present in ECE. Comparisons between observational as well reconstructed summer VPD and North Atlantic Oscillation (NAO) indices reveal significant relationships ($p<0.01$) in all four investigated regions (Table S4).

During the recent decades of the 21st century the moisture demand of the atmosphere increased to unusually high levels in three of our four reconstructions and the synchronicity of this increase was unprecedented in the 400-year context (Fig. 3). This increase has continued until 2020 to a level not reached in the previous 400 years across WE, ECE and most strongly AP, whereas in SF it was less pronounced. Within this recent period, particularly high VPD levels have been reached during the European drought years of 2003, 2015 and 2018, that affected all four regions.

Comparison of our reconstructions plus observations with summer VPD simulations from twelve available Earth system models[33] (ESM) enabled independent confirmation of the unprecedented VPD increase of the recent 30-year period (1991-2020) and its attribution to human influence. Three main types of simulations were considered: i) simulations forced with pre-industrial conditions, ii) simulations including both natural and anthropogenic historical forcing until 2014, and iii) simulations including a scenario of medium future greenhouse gas forcings (see methods).

Reconstructions and simulations agreed well in their distribution of normalized 30-year mean VPD values of the pre-industrial period (Fig. 4). More importantly, the multi-model means indicated with more than 98% probability in SF, WE and ECE, and with even higher probability in AP that VPD levels of the current 30-year period (1991-2020) could only be reached when attributing them to human influence. Multi-model means simulated with historical natural forcing excluding human influence were still well within the estimated ranges of pre-industrial variability (Table S5). Although individual ESMs simulations varied notably, with some of them simulating recent VPD values as high as the observations and others even lower than the pre-industrial average (Fig. 4; Table S6), results from multi-model means were consistent. Observed normalized summer VPD means of the recent 1991-2020 period strongly exceeded pre-industrial values and were substantially higher than the multi-model means in all four target regions (Table S7). In comparison recent non-normalized VPD levels from the multi-model means generally agreed well with the levels of the observations (Fig. S8). Sensitivity tests confirmed that our findings are robust i) when analysing 10-year instead of 30-year means (Fig. S9), ii) when estimating the baseline climate variability of pre-industrial VPD from consecutive non-overlapping periods in the simulations, instead of randomly sampled years (Fig. S10), and iii) when using model simulations that exclude the influence of past land use/land cover (LULC) on recent VPD (Table S8, supplementary text).

Discussion

Increase in European summer VPD is unprecedented and human-induced

Summer drying of the atmosphere intensified in the recent decades and significantly exceeded pre-industrial conditions of the past 400 years across all European target regions, as indicated by a combination of tree-ring $\delta^{18}O$ based reconstructions, gridded meteorological observations, and ESM simulations. The magnitude of the recent increase and the absolute VPD levels reached vary, however, among our four target regions. Strongest atmospheric drying trends are seen in the southern, continental mountain regions of the Alps & Pyrenees, followed by the temperate lowlands of western and eastern Central Europe, whereas in southern Fennoscandia, this trend is less pronounced. Model simulations further demonstrate that the observed summer VPD level of the last 30 years would have been extremely unlikely to occur without ongoing human-induced climate change.

Regional patterns of the summer VPD increase and potential drivers

Some synchronized periods of historical low and high atmospheric moisture demand across Europe in our reconstructions, together with dipole-like spatial correlation fields and significant relationships to NAO indices (Table S4, supplementary text) indicate a link between VPD and large-scale climate dynamics. The latitudinal position of the North Atlantic Jet Stream during summer and the corresponding occurrence and duration of near-stationary atmospheric pressure fields (“atmospheric blocking”) have been reported as major drivers of historical and recent dry and moist weather regimes over the North Atlantic-European domain[34,35,36] and recently even as drivers of forest productivity across Europe[34]. Also, the increasing number of mid-latitude weather extremes in the recent decades have been associated with an enhanced latitudinal variability of the North Atlantic Jet[35]. Such large-scale atmospheric modes could also serve as an explanation for the extreme year 1709 with outstandingly low reconstructed VPD values of the full 400-year study period (except in AP). An exceptionally strong negative NAO phase has been reported for this year[36], with the most severe frost conditions of the past 500 years continuing even into early summer and extending widely across the European continent[36,37]. Late soil thawing and ^{18}O-depleted “cold” precipitation together with low atmospheric demand far into the growing season have allowed propagating this extreme event specifically into tree-ring $\delta^{18}O$ (but not into European-scale growth-based and combined $\delta^{13}C$-$\delta^{18}O$ chronologies respectively, Fig. S7 and references therein).

Regional differences in the magnitude of the most recent VPD increase are interpreted here towards the nonstationary evolution of the actual vapor pressure in the air and an intensification of the water cycle under recent warming due to land–ocean-atmosphere feedback processes[2,3,38]. In Fennoscandia, an increase in atmospheric moisture has been reported over the past 30 years and can be specifically linked to changes in the dynamic processes of moisture supply from the oceanic source regions, such as increasing ocean evaporation[38] explaining the moderate increase in VPD observed there. In western and eastern central Europe and even more towards southern and continental regions such as the Alps & Pyrenees, a recent decrease in relative air humidity has been reported that is to a certain degree related to stronger differences between faster increasing air temperatures over land masses and slower increasing sea surface temperatures in the oceanic moisture region[2,38]. Therefore, humidity of the air advected from oceans to land surfaces would not increase enough to maintain a constant e_a in these continental regions[39]. The combination of increasing temperatures and constant or even decreasing e_a intensifies the desiccation strength of the atmosphere beyond the effect of warming alone.

Ecological and socio-economic implications

Our reported increase in VPD to the unprecedented levels of the recent years has major implications for land-atmosphere interactions, vegetation dynamics and carbon budgets, depending on the climatic region. In continental and Mediterranean areas declines in stomatal conductance driven by increasing atmospheric VPD lead to decreased evapotranspiration and thus to a further enhancement of air drying[4] and can already represent a significant constraint on plant carbon uptake[40]. Considering that forest canopy leaves are typically warmer than air and have limited ability to regulate temperature[41], a leaf-specific VPD increase may even exceed the increase in atmospheric VPD, with amplification of reduced carbon assimilation capacity and eventually heat damage. In other regions such as western and eastern central Europe an increase of tree-ring $\delta^{18}O$ sensitivity to summer VPD over the recent decades indicates continued high stomatal conductance and an amplification of evapotranspiration[42,43,44] in correspondence with a large-scale intensification of the atmospheric moisture demand[43,45], and as a consequence, the hydrological cycle[2].

Recent studies already report a response shift of vegetation growth towards increased sensitivity to VPD in the last few decades[46,47,48], including reductions in gross primary productivity[49], increased tree mortality[13,50], forest decline and yield reductions[6]. A further increase in VPD will cause enhanced wildfire risk, modify wildfire regimes, and may transform regions that are currently fire-free into fire prone ecosystems[3] such as the Pyrenees[51] as one of our study regions.

Our findings may be viewed within the context of the recent increase in wildfires and extreme drought-related events across many parts of Europe. If the atmosphere continues to dry, we would anticipate impacts on natural ecosystem services, the forestry and agricultural sector and human health. In turn, increased evaporation and associated changes in the amount and distribution of precipitation will disrupt water management infrastructure, affecting the availability, distribution and quality of water, as well as the reliability of the resource for hydropower generation, irrigation and human use. The direct and indirect effects of a drying atmosphere are likely to be far reaching and will require attention to minimize their future negative impacts.

Methods

European network of tree-ring $\delta^{18}O$ records

A network of 45 sites with tree-ring cellulose $\delta^{18}O$ chronologies across Europe was established (Table S1) using data primarily from the two EU-funded projects ISONET (20 sites) and Millennium (15 sites), and the Swiss Sinergia project iTREE (6 sites). Four additional data sets were downloaded from the NOAA paleoclimate database (‘Ang’ and ‘Fon’[52], ‘Ger’[53]; ‘Cze’[15]).

The sampling design considered temperate lowland sites, with tree growth governed by a complex combination of environmental factors and also ecologically extreme high elevation sites where few climatic factors dominate tree growth[16] (Table S1). Sites range from 5 to 2200 m elevation, with the majority situated in two elevation bands: 0–500 m and 1500–2200 m. High-altitude sites are concentrated in the south of the network. The network is dominated by oak and pine species (16 and 17 sites respectively), but also contains 5 spruce, 3 beech, 2 larch, 1 juniper and 1 cedar site (Table S1). At each location the most abundant and long-lived trees were selected and at least four dominant trees per site were used for isotope analysis (1-2 cores per tree). In general, oak $\delta^{18}O$ measurements were performed on latewood (except CAV, where no separation in early and latewood was possible owing to particularly narrow growth rings), while whole tree rings were analysed for beech and conifers (supplementary text).

Tree-ring widths were measured and cross-dated following standard procedures to ensure correct dating of each annual ring. Individual rings were separated with a scalpel under a microscope. At some sites, tree rings from the same year were pooled prior to cellulose extraction, while at others individual trees were measured and averaged to site chronologies. For iTREE, 5-7 dominant and 5 suppressed trees were analysed at each site[19], but for consistency with other sites, we developed chronologies using the dominant trees only. Cellulose was extracted using standard techniques[54]. Oxygen isotope analysis was conducted on CO obtained from pyrolising the samples in elemental analysers and measurements with isotope-ratio mass-spectrometry[54]. Isotope values are given as δ-values calculated from the isotope ratios $^{18}O/^{16}O$ (=R) as $\delta^{18}O = (R_{sample}/R_{standard} - 1) * 1000$ ‰ (referring to the international standard VSMOW) and have a long-term estimated methodological error of <0.2 ‰. The lengths of the chronologies varied from 95 years ('Tur' and 'San') to 1500 years ('Cze) with a median chronology length of 288 years. Our study was restricted to the past 415 years, back to 1600 CE.

Four datasets were downloaded from the NOAA Paleoclimatology database, i.e., two French chronologies[52], one of them Fontainebleau (Fon) replacing and extending the previous chronology established in ISONET, and Angoulême (Ang). The new Fon chronology, provided as $\delta^{18}O$ anomalies only, was scaled to the 20th century mean of the previous Fon chronology, and Ang was scaled to the mean of the old trees at this site[52]. For the Spanish dataset Gerber (Ger)[53] the mean was calculated of all five individual tree series, even though the mean inter-series correlation was relatively low (mean $r_{1901\text{-}2009}$ = 0.22). For 'Cze'[15] all $\delta^{18}O$ data were selected that reach back to 1600 CE, including living trees and relict wood from several locations in the Czech Republic. Due to offsets between individual measurements, the chronology was generated by calculating anomalies from the mean of each individual data set and averaging them after.

All site $\delta^{18}O$ records were screened for missing values and gaps filled based on information from adjacent chronologies using the software program ARSTAN (Cook et al. 2017). Furthermore, all chronologies were tested for potential artificial, non-climatic long-term trends for example possibly caused by pooling multiple trees. The general absence of such trends (except the early portions of Col, Ser, and Ped, which did not reach 75% membership component during fuzzy cluster analysis, see below) is in line with other studies[20,21,22] and allowed for further analyses using the non-detrended data.

Spatial clustering and regional principal components

Fuzzy cluster analysis[55,56] was applied for the period 1920-1994 CE on the raw tree-ring $\delta^{18}O$ chronologies with the aim to identify regional groups across the network. Contrary to hard clustering, fuzzy clustering allows data to belong to more than one cluster with membership grades assigned to each of the data points. These membership grades indicate the degree to which data belong to each cluster. The number of clusters is defined by maximizing the correlation between sites within each cluster over the 1920-2000 period. The best correlation was obtained with five clusters representing distinct geographic regions (A&P, WE, ECE, SF and NF). The membership exponent (membership in %) was used to identify the strength of contribution of the individual site chronologies to the common variance of the cluster. Only site chronologies exceeding a membership exponent threshold of 75% were selected for the development of regional time series for climate reconstruction (Fig. S5).

To create such regional time series, we applied nested principal component analysis[57] for each cluster separately. Since the number of available chronologies decreases back in time, all tree-ring $\delta^{18}O$ predictors within a given time period were used to generate a principial component regression model, then the shortest chronology/ies were removed and a new model was generated with the remaining chronologies. This nesting approach was repeated back in time and resulted in a varying number of 'nests' per cluster back through time (Table S3). The first principal component (PC1) was calculated for each cluster and the PC1 factors of the individual nests per cluster spliced together after scaling to VPD. The variance explained by PC1 of the individual nests varied between 46% and 61% for western Europe (five nests), between 62% and 64% for eastern central Europe (four nests), between 58% and 61% for the Alps & Pyrenees (five nests), between 55% and 62% for southern Fennoscandia (four nests), and between 38% and 45% for northern Fennoscandia (three nests).

Calibration, verification and VPD reconstruction

After normal distribution of the raw tree-ring $\delta^{18}O$ data as well as the PC1 nests was confirmed by the Shapiro normality test, Pearson's correlation coefficients between tree-ring $\delta^{18}O$ records and climate variables were calculated. This was done for each individual raw site $\delta^{18}O$ chronology on a site-by-site basis as well as for each of the nested PC1 records developed for the five regional clusters using the 0.5° x 0.5° monthly gridded meteorological dataset of the Climate Research Unit, University of East Anglia, UK (CRU TS4.05)[58]. Analyses considered 11 monthly variables, i.e., mean (T_{mean}), minimum (T_{min}) and maximum (T_{max}) temperatures, precipitation sums (PPT), standardized precipitation evapotranspiration index (SPEI), cloud cover (CLD), wet day frequencies (WET), potential evapotranspiration (PET), vapor pressure (VP), water balance (WAB, calculated as precipitation minus potential evapotranspiration) and, most importantly, atmospheric vapor pressure deficit (VPD). VPD was calculated as saturated minus actual vapor pressure with the latter available as a standard CRU dataset, whereas the former was derived from CRU T_{mean} data using the formula $VP_{sat} = 6.11*10^{((7.5*T)/(237.3+T)}$[59].

The period 1920-2000 was defined as the core period for calibration due to some irregularities in the available climate data prior to 1920 (e.g., abrupt changes in magnitude or variance) and reduced replication of the composite $\delta^{18}O$ records in the most recent period. In a first step, monthly correlations were calculated from March of the year before tree-ring formation to October of the year of tree-ring formation and for 186 combinations of months using the closest gridpoint to identify the seasonality in the climate response at each site. Calculations were performed in R using the python module rpy2 (R version 3.5.1, Python version 3.7., rpy2 version 2.9.5) (https://rpy2.github.io).

Spatial correlation fields for each of the five sub-regions were calculated based on the gridded VPD dataset of June to August (JJA). All VPD gridpoints revealing significance of the correlation coefficients at $p<0.001$ with the corresponding regional PC1 record were averaged and this mean used as target for climate reconstruction prior to the instrumental period.

Calibration/verification statistics such as explained variance (R^2), reduction of error (RE), coefficient of efficiency (CE) and Durbin-Watson test (DW) were applied to each individual PC1 nest to quantify the signal strength and the temporal robustness of the reconstructions. The goodness of the fit between the PC1 records of the different sub-regions and regional summer VPD was assessed by correlation, comparing the linear trends of the regression residuals and the Durbin–Watson statistic – a measure of the persistence in the residuals of a regression (between proxy and station data) (Table S3). Climate variability, i.e., variability of summer VPD prior to the instrumental period was reconstructed by scaling each spliced regional PC1 nest to the same mean and variance as its corresponding VPD observational record over the full 1920-2000 calibration period.

VPD simulations from Earth system models

The monthly data output from twelve Earth system models (ESMs) from the sixth phase of the Coupled Model Intercomparison Project (CMIP6)[33] with extracted data corresponding to the spatial coverage of our reconstructions plus observations were utilized for simulations of summer VPD: ACCESS-ESM1-5, CESM2, CMCC-ESM2, CNRM-ESM2-1, CanESM5, EC-Earth3-Veg, GFDL-ESM4, IPSL-CM6A-LR, MIROC-ES2L, MPI-ESM1-2-LR, MRI-ESM2-0, and UKESM1-0-LL. The model selection was based on the availability of the required output variables of temperature and relative humidity for the different types of simulations used in our study. Only one model version per model family was selected to avoid biasing the multi-model mean to those model families with more versions available.

Three main types of simulations were considered for the analyses: “piControl”, “historical” and “ssp245”, while using one ensemble member per model. The “piControl” scenario was used to estimate natural climate variability with simulations including external natural forcing (i.e., volcanic eruptions, solar irradiance variability) while keeping anthropogenic forcing constant (i.e., human-induced changes to CO_2 concentration, aerosols, land use etc.) at pre-industrial conditions. In contrast, “historical” simulations (1850-2014) include both natural and anthropogenic radiative forcing. For the analyses with respect to the period 1991-2020, we combined the "historical" simulations extending until 2014 with simulations from the "ssp245" scenario during 2015 to 2020, an intermediate scenario that is closest to emissions implied by current policies. Furthermore, we conducted additional tests using “hist-nat” simulations including historical (1850-2020) natural forcing and excluding anthropogenic forcing (Table S5), as well as “hist-noLu” simulations which are similar to the “historical” simulations but keep land use/land cover constant at pre-industrial conditions (Table S8, supplementary text).

As for the observations, VPD was calculated as saturated minus actual vapor pressure: $VPD_{sat} = 6.11*10^{((7.5*T)/(237.3+T))}$; $VPD_{act} = VPD_{sat}$*relative humidity/100. For these calculations near-surface air temperature and relative humidity were used from all models. For each year the average of the 3-month period June–August was computed.

We note that all estimates were first computed for each CMIP6 ESM at every grid cell (~2°x2° depending on each model) and were then area-weighted averaged to the same regional scale of the corresponding reconstructions. Time series of normalized VPD are shown in Fig. S10 and the interannual variability from the "piControl" simulations are provided in Table S5. We note that the interannual variability of the reconstruction during 1600 to 1849 is generally lower than that of the ESMs across all four analysed regions.

Attribution of VPD to human-induced climate change

To assess the human-induced climate change effects[32,60] on the observed summer VPD from 1991 to 2020, we compared it to the expected VPD from natural climate variability under pre-industrial atmospheric CO_2 conditions. To do so, we estimated an empirical distribution of 30-year mean VPD arising from natural climate variability by randomly sampling (without repeating years) 500 different 30-year subsets from the reconstruction between 1600 and 1850. In addition, we estimated the expected summer VPD from 1991 to 2020 based on historical ESM simulations with human-induced plus natural radiative forcing (combination of "historical" and "ssp245" type simulations), as well as the natural climate variability VPD distribution based on simulations with pre-industrial atmospheric forcing ("piControl" type simulations). To estimate the VPD variability from the piControl 500-year simulations we also randomly sampled (without repeating years) 500 different 30-year subsets. To allow comparability between the reconstruction and the ESMs, VPD was normalized by subtracting the mean and dividing by the interannual standard deviation of the entire pre-industrial period. As additional tests we also estimated recent summer VPD from simulations excluding anthropogenic forcing (“hist-nat”) and from simulations with land use/land cover kept constant at pre-industrial conditions (“hist-noLu”).

Data availability

The final summer VPD reconstructions will be freely available upon publication from the NOAA National Centre for Environmental Information (NCEI) together with the raw tree-ring $\delta^{18}O$ chronologies from the iTree project (see Table S1). Raw tree-ring $\delta^{18}O$ chronologies from the ISONET project are freely accessible here: ISONET Project Members et al. (2022): Stable oxygen isotope ratios of tree-ring cellulose from the site network of the EU-Project ‘ISONET’. GFZ Data Services. https://doi.org/10.5880/GFZ.4.3.2022.003. The remaining unpublished raw tree-ring $\delta^{18}O$ chronologies are currently under the stewardship of the individual data producers who may be contacted regarding their availability and collaborative access, prior to their future public archival.

The CMIP6 data used in this study are available at https://esgf-node.llnl.gov/search/cmip6/. Detailed inputs for the search query are as follows: source IDs are ACCESS-ESM1-5, CESM2, CMCC-ESM2, CNRM-ESM2-1, CanESM5, EC-Earth3-Veg, GFDL-ESM4, IPSL-CM6A-LR, MIROC-ES2L, MPI-ESM1-2-LR, MRI-ESM2-0, and UKESM1-0-LL; experiment IDs are piControl, historical and ssp245; variant label is r1i1p1f1 or the next lowest number if unavailable for some models; frequency is mon; and variables are tas and hurs.

Code availability

R-codes used for chronology construction and statistical analyses will be made available upon request via the corresponding author.

Acknowledgments

We acknowledge the World Climate Research Programme's Working Group on Coupled Modelling, which is responsible for the Coupled Model Intercomparison Project (CMIP), and we thank the climate modeling groups for producing their model output and making it available. For the CMIP, the US Department of Energy's Program for Climate Model Diagnosis and Intercomparison provides coordinating support and led development of the software infrastructure in partnership with the Global Organization for Earth System Science Portals.

This study was funded by the EC projects ISONET EVK2-CT-2002-00147 and Millennium FP6-2004-GLOBAL-017008-2 and by the Swiss National Science Foundation (SNSF) projects iTREE CRSII3_136295 and TROXY 200021_175888 (SK, KT, EMS). Other funding included NASA’s Terrestrial Ecology program (BP), Slovenian Research Agency P4-0107 (TL, PH), MIUR-PRIN 2002 2002075152 & MIUR-PRIN 2005 2005072877 (AS, LT), PALEOMEX-ISOMEX program CNRS-INSU (VD), Fundació La Caixa through the Junior

Leader Program LCF/BQ/LR18/11640004 (IDL), ERC 755865 & Academy of Finland 295319 (KR-G), Czech Science Foundation CZ.02.1.01/0.0/0.0/16_019/0000797 (UB, JE), Spanish Ministry of Science and Technology REN2002-11476-E/CLI (EG), and ERC AdG 882727 (JE), UKRI EP/X025098/1 (NJL). L.L., R.P., and S.I.S. acknowledge support from the European Union's Horizon 2020 Research and Innovation Program (grant agreement 821003 (4C)). Comments of William Lukens and two anonymous reviewers helped to improve the manuscript. The views and conclusions contained in this document are those of the authors and should not be interpreted as representing the opinions or policies of the funding agencies and supporting institutions.

Author contributions

K.T., L.L., R.P., F.B., D.C.F., A.Ka., S.I.S. and N.J.L. designed the research; K.T., L.L., R.P., F.B., D.C.F., E.M.-S., B.P. and R.W. performed the research with imput from A.G., A.Ka., A.Ke., A.S. and S.I.S.. K.T. wrote the paper. All listed authors from L.A.-H. to G.Y. were involved in data production and provided feedback on the manuscript.

References

1. Bohren, C. F., Albrecht, B. A., Schroeder, D. V. Atmospheric thermodynamics. *American Journal of Physics* **68**, 1159–1160 (2000).
2. Douville, H. et al. Water Cycle Changes. In Climate Change 2021: The Physical Science Basis. Contribution of Working Group I to the Sixth Assessment Report of the Intergovernmental Panel on Climate Change [Masson-Delmotte, V. et al. (eds.)]. Cambridge University Press, Cambridge, United Kingdom and New York, NY, USA, 1055–1210 (2021).
3. Seneviratne, S. I. et al. Weather and Climate Extreme Events in a Changing Climate. In: Climate Change 2021: The Physical Science Basis. Contribution of Working Group I to the Sixth Assessment Report of the Intergovernmental Panel on Climate Change [Masson-Delmotte, V. et al. (eds.)]. Cambridge University Press, Cambridge, United Kingdom and New York, NY, USA, 1513-1766 (2021).
4. Seneviratne, S. I. *et al*. Investigating soil moisture–climate interactions in a changing climate: A review. *Earth-Science Reviews* **99**, 125–161 (2010).
5. Grossiord, C. et al. Plant responses to rising vapor pressure deficit. *New Phytol*. **226**, 1550–1566 (2020).
6. Hsiao, J. et al. Maize yield under a changing climate: The hidden role of vapor pressure deficit. *Agric. For. Meteorol*. **279,** 107692 (2019).
7. Ranasinghe, R. et al. Climate Change Information for Regional Impact and for Risk Assessment. In Climate Change 2021: The Physical Science Basis. Contribution of Working Group I to the Sixth Assessment Report of the Intergovernmental Panel on Climate Change [Masson-Delmotte, V. et al. (eds.)]. Cambridge University Press, Cambridge, United Kingdom and New York, NY, USA, 1767–1926 (2021).
8. Yuan, W. et al. Increased atmospheric vapor pressure deficit reduces global vegetation growth. *Sci. Adv.* **5**, eaax1396 (2019).
9. Miralles, D. G., Gentine, P., Seneviratne, S. I., Teuling, A. J. Land–atmospheric feedbacks during droughts and heatwaves: state of the science and current challenges. *Ann. N.Y. Acad. Sci.* **1436**, 19–35, doi: 10.1111/nyas.13912 (2019).
10. Ficklin, D. L. & Novick, K. A. Historic and projected changes in vapor pressure deficit suggest a continental-scale drying of the United States atmosphere. *J. Geophys. Res. Atm.* **122**, 2061–2079 (2017).
11. Humphrey, V. et al. Soil moisture–atmosphere feedback dominates land carbon uptake variability. *Nature* **592**, 65–69 (2021).
12. Fu, Z. et al. Atmospheric dryness reduces photosynthesis along a large range of soil water deficits*. Nature Comm.* **13**, doi.org/10.1038/s41467-022-28652-7 (2022).
13. Breshears, D. D. et al. The critical amplifying role of increasing atmospheric moisture demand on tree mortality and regional die-off. *Front. Plant Sci.* **4**, 266, doi10.3389/fpls.2013.00266 (2013).
14. Clarke, H. et al. Forest fire threatens global carbon sinks and population centres under rising atmospheric water demand. *Nature Comm*. **13**, 10.1038/s41467-022-34966-3

(2022).

15. Büntgen, U. et al. Recent European drought extremes beyond Common Era background variability. *Nature Geoscience* https://doi.org/10.1038/s41561-021-00698-0 (2021).
16. Treydte, K. et al. Signal strength and climate calibration in a European tree-ring isotope network. *Geophys. Res. Lett*. **34**, L24302, doi:10.1029/2007GL031106 (2007).
17. Treydte, K. et al. Impact of climate and CO_2 on a millennium-long tree-ring carbon isotope record. *Geochim Cosmochim. Acta* **73**, 4635-4647 (2009).
18. D. McCarroll et al. Correction of tree ring stable carbon isotope chronologies for changes in the carbon dioxide content of the atmosphere. *Geochim. Cosmochim. Acta* **73**, 1539–1547 (2009).
19. Klesse, S. et al. Oxygen isotopes in tree rings are less sensitive to tree size and stand dynamics than carbon isotopes. *Plant Cell Environ*. **41**, 2899-2914 (2018).
20. Young, G. H. F. et al. Age trends in tree ring growth and isotopic archives: A case study of *Pinus sylvestris* L. from northwestern Norway. *Glob. Biogeo. Cycles* **25**, doi10.1029/2010GB003913 (2011).
21. Duffy, J. E. et al. Absence of age-related trends in stable oxygen isotope ratios from oak tree rings. *Glob. Biogeo. Cycles* **33**, 841-848 (2019).
22. Büntgen, U. et al. No evidence of age trends in oak stable isotopes. *Paleooceanography and Paleoclimatology*, doi.org/10.1029/2019PA003831 (2020).
23. Gessler, A. et al. Stable isotopes in tree rings - Toward a mechanistic understanding of isotope fractionation and mixing processes from the leaves to the wood. *Tree Physiol.*, doi10.1093/treephys/tpu040 (2014).
24. Treydte, K. et al. Seasonal transfer of oxygen isotopes from precipitation and soil to the tree ring: Source water versus leaf water enrichment. *New Phytol.* **202***,* 772-783 (2014).
25. Sternberg, L., Pinzon, M. C., Anderson, W. T., Jahren, A. H. Variation in oxygen isotope fractionation during cellulose synthesis: intramolecular and biosynthetic effects. *Plant Cell Environ.* **29**, 1881–1889 (2006).
26. Martinez-Sancho, E., et al. Unenriched xylem water contribution to cellulos synthesis influenced by atmospheric demand governs the intra-annual tree-ring d18O signature. New Phyt. Close to acceptance (2023).
27. Levesque, M. et al. Tree-ring isotopes capture interannual vegetation productivity dynamics at the biome scale. *Nature Comm.* **10**, 742 (2019).
28. Daux, V. et al. Comparisons of the performance of $\delta^{13}C$ and $\delta^{18}O$ of *Fagus sylvatica*, *Pinus sylvestris*, and *Quercus petraea* in the record of past climate variations. *J. Geophys. Res. Biogeosci.* **123**, 1145–1160. https://doi.org/10.1002/ 2017JG004203 (2018).
29. Vitali, V. et al. High-frequency stable isotope signals in uneven-aged forests as proxy for physiological responses to climate in Western Europe. *Tree Physiol.* **41**, 2046-2062 (2021).

30. Naulier, M. et al. A millennial summer temperature reconstruction for northeastern Canada using oxygen isotopes in subfossil trees. *Clim. Past* **11**, 1153–1164 (2015).
31. Field, R. D. et al. Tree-ring cellulose $\delta^{18}O$ records similar large-scale climate influences as precipitation $\delta^{18}O$ in the Northwest Territories of Canada. *Climate Dynamics* **58**, 759-776 (2022).
32. Padrón, R.S. et al. Observed changes in dry-season water availability attributed to human-induced climate change. *Nature Geoscience* **13**,477-481 (2020).
33. Eyring, V. et al. Overview of the Coupled Model Intercomparison Project Phase 6 (CMIP6) experimental design and organization. *Geosci. Model Dev.* **9**, 1937–1958 (2016).
34. Dorado-Liñán I. et al. Jet stream position explains regional anomalies in European beech forest productivity and tree growth. *Nature Comm*. **13**, 2015 (2022).
35. Trouet, V., Babst, F., Meko, M. Recent enhanced high-summer North Atlantic Jet variability emerges from three-century context. *Nature Comm.* **9,** 180 (2018).
36. Luterbacher, J., Dietrich, D., Xoplaki, E., Grosjean, M., Wanner, H. European Seasonal and Annual Temperature Variability, Trends, and Extremes Since 1500. *Science* **303**, 1499-1503 (2004).
37. Derham, W. The history of the great frost in the last winter 1703 and 1708/9. *Philosophical Transactions* **26**, 454–478 (1709).
38. Vicente-Serrano, S. M. et al. Recent changes of relative humidity: regional connections with land and ocean processes. *Earth Syst. Dynam*. **9**, 915–937 (2018).
39. Sherwood, S. & Fu, Q. A drier future? *Science* **343**, 737–739 (2014).
40. McDowell, N. G. et al. Mechanisms of woody-plant mortality under rising drought, CO_2 and vapour pressure deficit. *Nature Rev. Earth Environ.* ttps://doi.org/10.1038/s43017-022-00272-1 (2022).
41. Still, C. J. et al. No evidence of canopy-scale leaf thermoregulation to cool leaves below air temperature across a range of forest ecosystems. *PNAS*, doi.org/10.1073/pnas.2205682119 (2022).
42. Lansu, E. M., van Heerwaarden, C. C., Stegehuis, A. I., Teuling, A. J. Atmospheric aridity and apparent soil moisture drought in European forests during heat waves. *Geophys. Res. Lett.* **47**, e2020GL087091 (2020).
43. Zhao, M., Geruo, A ., Liu, Y., Kronings, A. G. Evapotranspiration frequently increases during droughts. *Nature Clim. Change* **12**, 1024–1030 (2022).
44. Vicente-Serrano, S. M., McVicar, T. R., Miralles, D. G., Yang, Y., Tomas-Burguera, M. Unraveling the influence of atmospheric evaporative demand on drought and its response to climate change. *WIREs Clim. Change*, doi/10.1002/wcc.632 (2020).
45. Li, S. et al. Attribution of global evapotranspiration trends based on the Budyko framework. *Hydrol. Earth Syst. Sci*. **26**, 3691–3707 (2022).
46. Novick, K. A. et al. The increasing importance of atmospheric demand for ecosystem water and carbon fluxes. *Nature Clim. Change* **6**, 1023 (2016).
47. Babst, F. et al. Twentieth century redistribution in climatic drivers of global tree growth. *Sci. Adv.* **5**, eaat4313 (2019).

48. Trotsiuk, V. et al. Tree growth in Switzerland is increasingly constrained by rising evaporative demand. *J. Ecol* **1.09**, 2981-2990 (2021).
49. Zhang, Q. et al. Response of ecosystem intrinsic water use efficiency and gross primary productivity to rising vapor pressure deficit. *Environ. Res. Lett.* **14**, 074023 (2019).
50. Allen, C. D., Breshears, D. D., McDowell, N. G. On underestimation of global vulnerability to tree mortality and forest die-off from hotter drought in the Anthropocene. *Ecosphere* **6**, 1-55 (2015).
51. de Dios, V.R. et al. Climate change induced declines in fuel moisture may turn currently fire-free Pyrenean mountain forests into fire-prone ecosystems. *STOTEN* **797**, 149104 (2021).
52. Labuhn, I. et al. French summer droughts since 1326 CE: a reconstruction based on tree ring cellulose, *Clim. Past* **12**, 1101–1117 (2016).
53. Konter, O. et al. Climate sensitivity and parameter coherency in annually resolved $\delta^{13}C$ and $\delta^{18}O$ from *Pinus uncinata* tree-ring data in the Spanish Pyrenees. *Chem. Geol.* **377**, 12–19 (2014).
54. Boettger, T. et al. Wood cellulose preparation methods and mass spectrometric analyses of $\delta^{13}C$, $\delta^{18}O$, and nonexchangeable $\delta^{2}H$ values in cellulose, sugar, and starch: An interlaboratory comparison. *Analytical Chemistry* **79,** 4603–4612 (2007).
55. Maechler, M., Rousseeuw, P., Struyf, A., Hubert, M., Hornik, K. cluster: Cluster Analysis Basics and Extensions. R package version 2.1.3, https://CRAN.R-project.org/package=cluster, (2022).
56. Kaufman, L., & Rousseeuw, P. J. Finding Groups in Data - An Introduction to Cluster Analysis. New York, Wily & Sons Inc. doi.org/10.1002/9780470316801 (1990).
57. Frank, D. C. & Esper, J. Temperature reconstructions and comparisons with instrumental data from a tree-ring network for the European Alps. *Int. J. Clim*. **25**, 1437-1454 (2005).
58. Harris, I. et al. Version 4 of the CRU TS monthly high-resolution gridded multivariate climate dataset. *Sci. Data* **7**, 109 (2020).
59. Murray, F. W. On the computation of saturation vapor pressure. *J. Appl. Meteorol.* **6**, 203-204 (1967).
60. Grant, L. et al. Attribution of global lake systems change to anthropogenic forcing. *Nature Geoscience* **14**, 849-854 (2021).

Figures and Tables

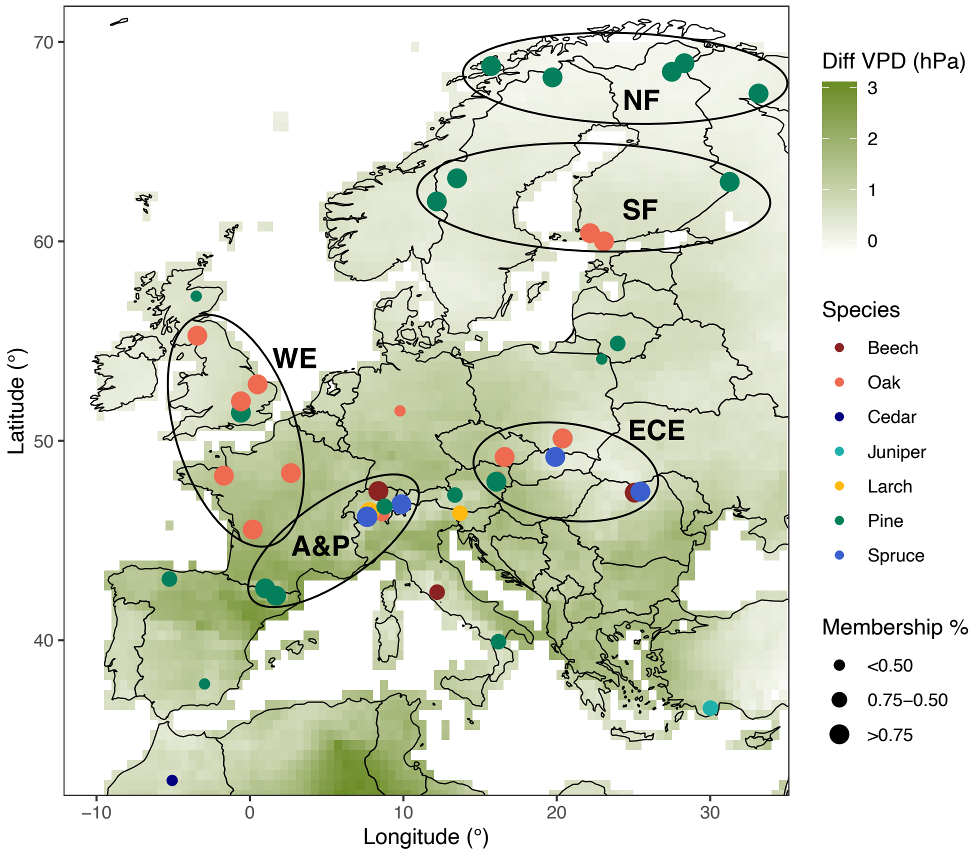

Figure 1. Distribution of 45 tree-ring cellulose δ^{18}O chronologies across Europe, spatial clustering and changes in observed European summer VPD. Dot sizes display membership in % of the individual site chronologies in a given cluster based on fuzzy cluster analysis (see also Fig. S4). The chronologies are separated into five independent target regions, i.e., northern Fennoscandia (NF), southern Fennoscandia (SF), western Europe (WE), eastern central Europe (ECE) and Alps & Pyrenees (AP). Green shadings represent differences in mean observational VPD between the period 1920-1990 and 1991-2020 calculated for each grid point.

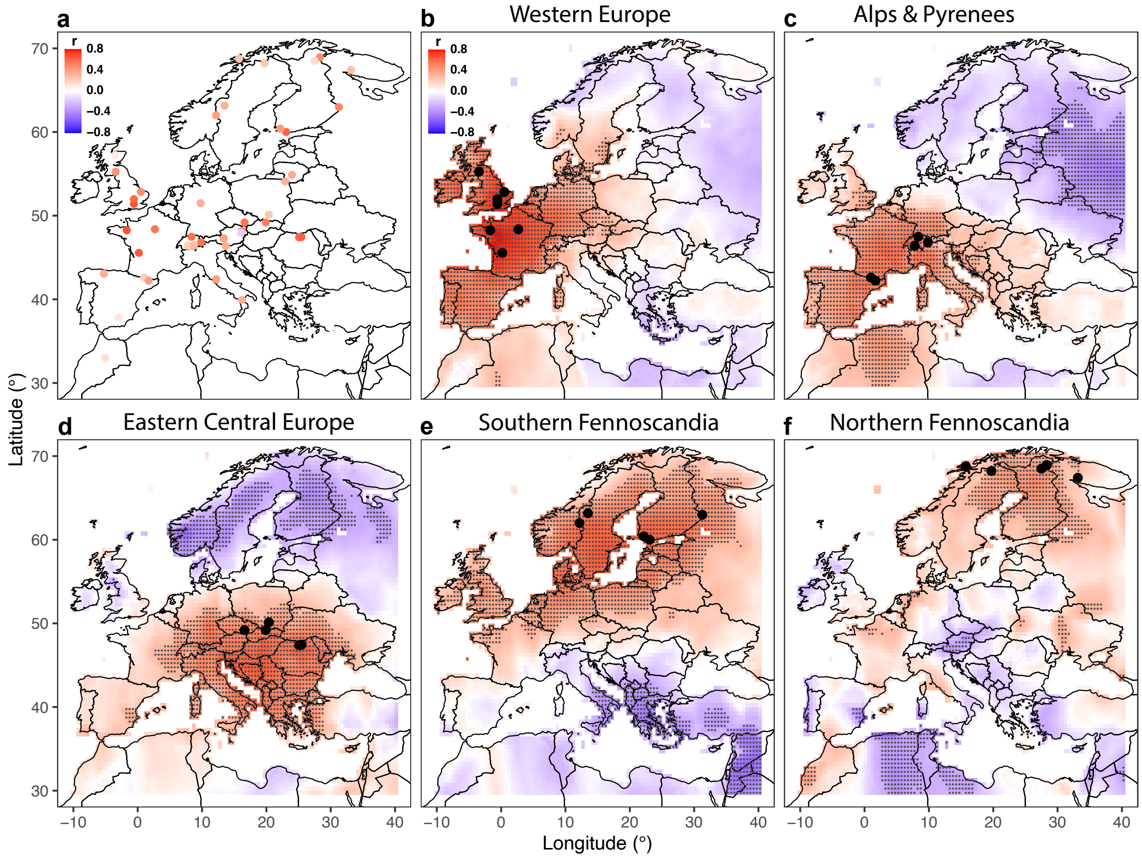

Figure 2. Spatial extend of the summer VPD signal in five European target regions. a) Correlation between individual site $\delta^{18}O$ chronologies and the closest summer VPD gridpoint. b-f) Spatial correlation fields calculated between the PC1 nests representing each of the five geographical regions derived from cluster analysis and gridded summer VPD (June-August). Large black dots indicate sites contributing to the corresponding PC1 nests of each regional cluster due to a membership exponent >75%, small black dots display grid points with significant correlations at $p<0.001$.

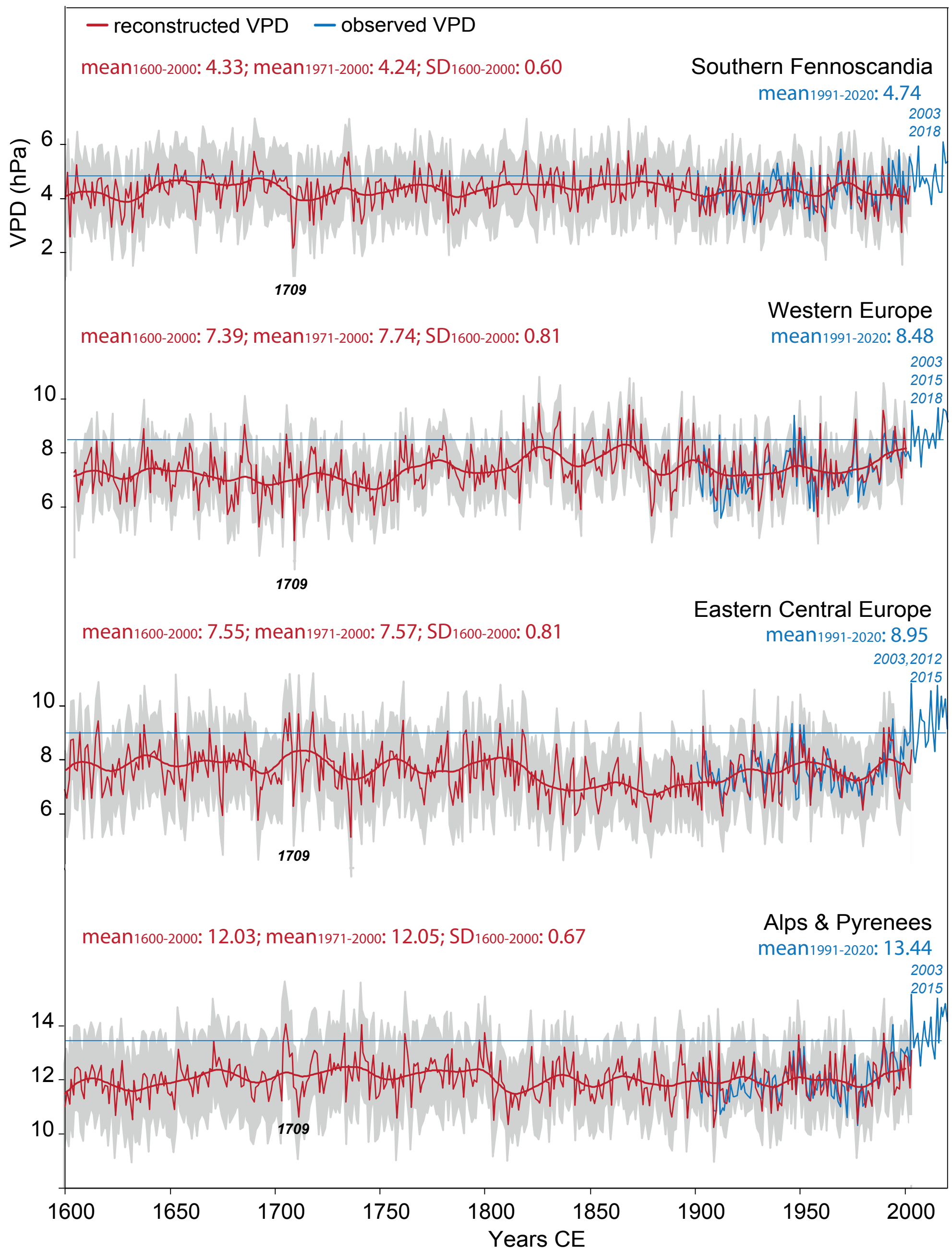

Figure 3. Reconstructed and observed summer (June-August) VPD for four European target regions. Horizontal blue lines indicate the mean of observed VPD for the period 1991-2020. Smoothed curves are 30-year splines with a frequency cut-off at 50%. Means and standard deviations (SD) are given in hPa. Grey areas indicate the root mean square error spliced together from the individual PC1 nests per region. Details on the robustness

of the δ[18]O-VPD relationships in the calibration period are provided in Fig. S5 and Table S3.

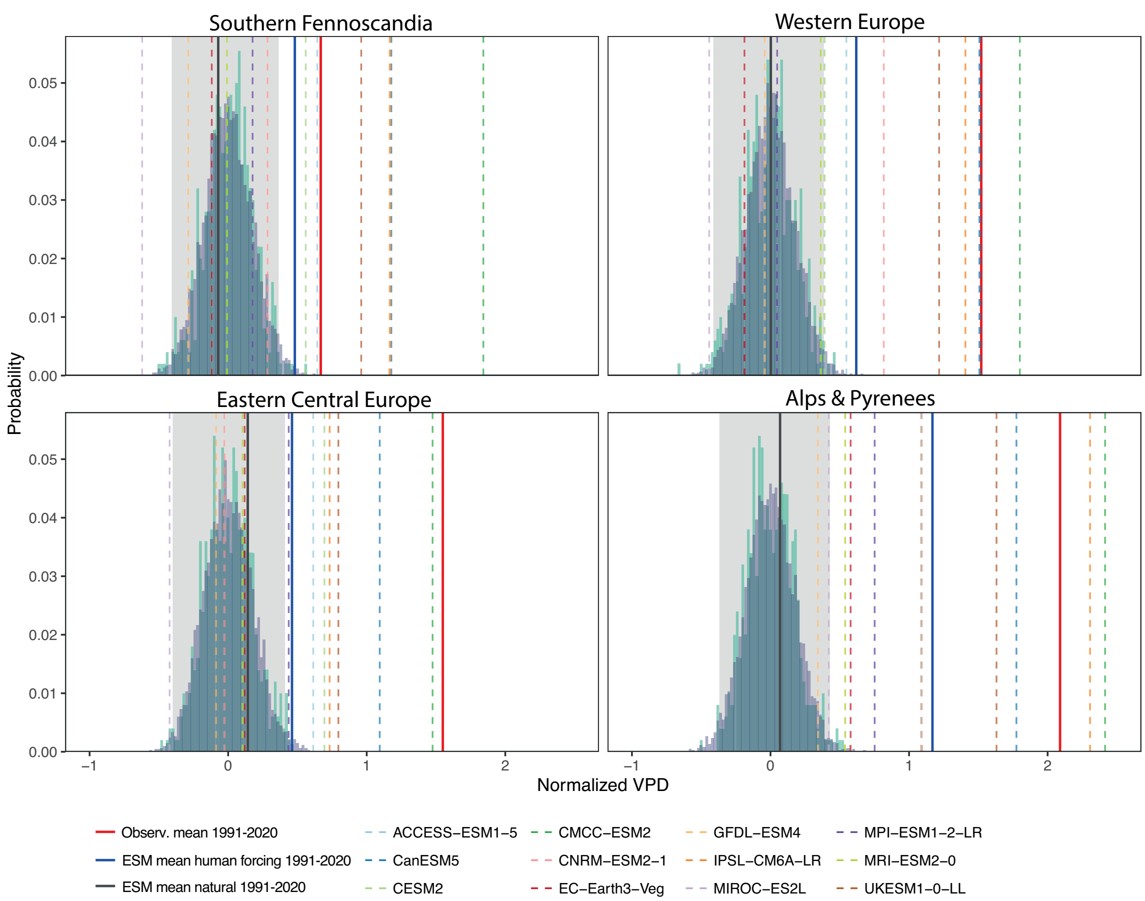

Figure 4. Unprecedented summer VPD increase in the context of pre-industrial natural variability and its attribution to human influence. Bars indicate pre-industrial natural variability from tree-ring δ[18]O-based VPD reconstructions for the period 1600-1850 (green), and from 500-year simulations of 12 ESMs with no human-induced forcing included, piControl (blue). Grey shadows indicate the 98% distribution range of natural variability. Solid lines indicate VPD during the most recent period 1991-2020 CE based on i) direct VPD observations (red), ii) multi-model means of combined historical and ssp245 scenarios with human-induced forcing included (blue), and iii) multi-model means of the historical scenario with human-induced forcing excluded (green). Dashed lines are the individual model means for 1991-2020 based on combined historical and ssp245 scenarios with human-induced forcing included. VPD values are normalized for comparability.